Interpretation of the magnetic anomalies over the Mid-Atlantic Ocean Ridge using Swarm-A satellite

Ilkin Özsöz [1] and *Oya Ankaya Pamukçu [2]*

[1] General Directorate of Mineral Research and Exploration, Marine Research Department, Ankara, Turkey

[2] Dokuz Eylul University, Engineering Faculty, Geophysical Engineering Department, İzmir, Turkey

The procedures and interpretation of the magnetic data measured over the Mid-Atlantic Ocean Ridge by Swarm-A satellite is discussed in this paper. The data processing procedure has four phases after the data format conversion. The first phase is the selecting data whose Kp index is lower than 1. Secondly, the main magnetic field should be subtracted from the measured data for example through the IGRF model. This step is followed by removing trend, related to the satellite trajectory. The final step is eliminating the dipole nature of the magnetic field via Reduction to the Pole (RTP). Nonetheless, the RTP process might cause misinterpretation over the large study area and lower latitudes. Therefore, the amplitude of the analytic signal (AS) is used as an alternative to the RTP. The qualitative interpretation of the magnetic anomaly is conducted via AS anomaly, bathymetry, heat flow and tectonic map. Quantitatively correlation coefficients of bathymetry and heat flow with respect to AS are interpreted.

Keywords: SWARM, magnetic data processing, analytic signal, qualitative and quantitative interpretation

1. Introduction

The magnetic survey is the most convenient and inexpensive method for investigation of the internal and external structure of Earth. The most featured advantage of the magnetic survey is that a large study area can be covered quickly and accurately by aeromagnetic or satellite data.

Recently, magnetic studies provided prominent information about Earth's crust (Langel and Hinze, 1998; Purucker and Whaler, 2007; Abramova et al., 2016). Geophysical exploration (Gibson and Millegan, 1998; Hildenbrand et al., 2000), large-scale geological interpretation and tectonic boundaries (Hinze, 1985)

can be evaluated via magnetic studies. Moreover, global magnetic field measurements shed light on the lithosphere-lower mantle interaction owing to the volcanic activity (Nakanishi et al., 1992; Roest et al., 1995; Bokelmann and Wustefeld, 2009).

Satellite magnetic data is widely used for the analysis of Earth's internal structure. Furthermore, magnetosphere and ionosphere can be investigated. Satellite data can provide uniform coverage for the global survey instead of unevenly distributed magnetic observatories.

Historically, there were four magnetic satellites, Pogo (Regan et al., 1975), Magsat (Langel et al., 1982; Cain et al., 1989; Arkani-Hamed et al., 1994; Ravat et al., 1995), Ørsted (Olsen, 2000) and CHAMP (Olsen et al., 2006; Maus et al., 2008; Abramova et al., 2016), which investigate parameters of the geomagnetic field.

The most recent magnetic satellite is SWARM (Friis-Christensen et al., 2006; Taylor et al., 2019), launched on 22 November 2013. and the European Space Agency operates the SWARM mission. SWARM mission includes three identical magnetic satellites, Swarm A, B and C. The initial altitudes of the lower two were 480 km and the higher one was 530 km.

Swarm satellites consist of both fluxgate vector magnetometer and Overhauser scalar magnetometer. Overhauser scalar magnetometer registers 86,400 measurements per day but the performance of the magnetometer can increased by burst mode which allows to collect 250 Hz data. On the other hand, fluxgate vector magnetometer collects 4,320,000 (50 Hz × 3600 s × 24 h) samples/day.

The latest previous studies showed that Swarm satellites can be used for monitoring electrical conductivity of the mantle (Civet et al., 2015), analysing the external magnetic field (Moretto et al., 2006), interpretation of regional total magnetic field (Taylor et al., 2014; Taylor et al., 2019), monitoring the magnetic field as an earthquake precursor (Akhoondzadeh, 2018).

The purpose of this paper is to interpret the regional total magnetic field of the lower, upper, Western and Eastern Mid-Atlantic Ocean Ridge (Fig. 1) and to determine an effective data processing scheme for Swarm magnetic data. In order to select magnetically quiet times and to obtaining the lithospheric magnetic field, the magnetic data has been edited, a linear trend has been removed and the phase has been corrected in the processing steps. Consequently, the regional magnetic field which reflects correct variations related to the magnetic properties of crust can be obtained.

2. Data processing methods

The Swarm magnetic data can be downloaded from either https://vires.services/ or https://swarm-diss.eo.esa.int (ESA/Swarm Level 1B folder). The data are given in CSV (Comma Separated Value) or CDF (Content
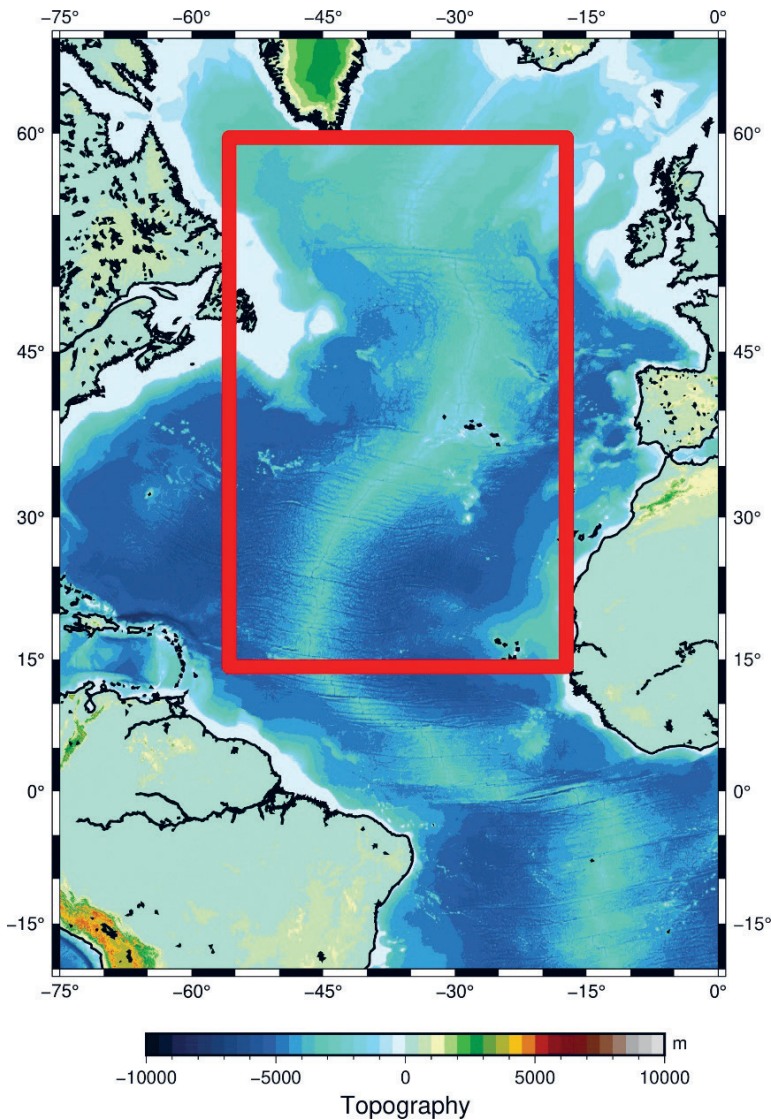
Figure 1. Location map for the study area (red rectangle).

Definition File) format. In this study data were downloaded from the VIRES platform and the data format was CSV. Timestamp of the downloaded data is from 10th October 2019 to 9th November 2019.

The first step is using the data which corresponds to the magnetically quiet time. Kp index describes solar wind disturbance on Earth's magnetic field and its range is between 0 and 9. Kp = 0, 1 and 2 correspond to quiet magnetic times
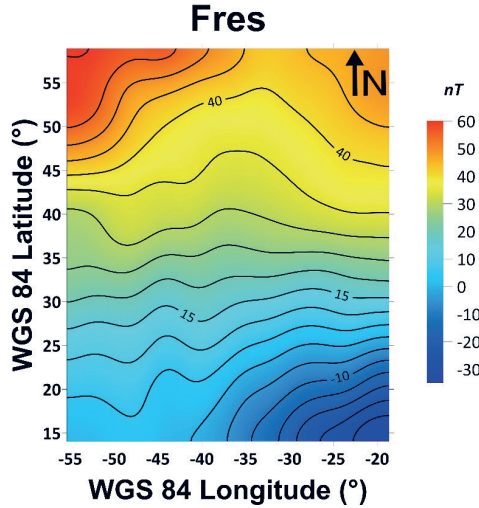
Figure 2. Residual magnetic field (*Fres*) after the IGRF model (*n* = 13) is subtracted.

(Mayaud, 1980). Threshold for the Kp index is chosen as 1. Namely, data with the Kp index is 1 and lower than 1 are selected for further steps. In this study, the restricted criterion is used for Kp index to remove any possible minor external disturbances which may produce artificial magnetic anomalies.

The second step is obtaining the total magnetic intensity anomaly which excludes main magnetic field of Earth (Fig. 2). It is known that the measured geomagnetic field is the superposition of the various components which are the main geomagnetic field which is generated by liquid part of the Earth's core, external magnetic field, induction field, seismo-induced phenomena, human-activities, electrical power lines and crustal magnetic field. In order to remove the magnetic field generated by Earth's liquid core, subtraction of the main field with geomagnetic model is required. To exclude external disturbance influences, only the magnetically quiet time is used. from the magnetically quiet times is used. Residual magnetic field (*Fres*) is obtained by subtracting an international analytical model (order *n* = 13), which is IGRF (Thébault et al., 2015), from each data points. IGRF model is calculated for time, longitude, latitude and altitude of each Swarm data sample.

The equation of the IGRF model for given time (t), geocentric co-latitude (θ), longitude (ϕ) and altitude (r) is:

$$V(r,\theta,\phi,t) = a \sum_{n=1}^{N} \sum_{m=0}^{n} \left(\frac{a}{r}\right)^{n+1} * \left[g_n^m(t)\cos(m\phi) + h_n^m(t)\sin(m\phi) \times P_n^m \cos(\theta) \right] \text{. (1)}$$

where r is the radial distance from the centre of the Earth and is reference radius of Earth (6,371.2 km). Furthermore, $P_n^m \cos(\theta)$ is Schmidt quasi-normalised

Legendre function (n and m are degree of the function) and g_n^m and h_n^m are Gaussian coefficients whose unit is nT. The first derivative respect to timestamp of the data (t) of Gaussian coefficients are given:

$$g_n^m(t) = g_n^m(T_0) + g_n'^m(T_0) * (t - T_0),$$ (2)

$$h_n^m(t) = h_n^m(T_0) + h_n'^m(T_0) * (t - T_0).$$ (3)

The first derivatives of the Gaussian coefficients ($g_n'^m(t)$ and $h_n'^m(t)$) are associated with mean linear variations for five 5 year period. Therefore, unit of these coefficients is nT/year. In equations (2) and (3), T_0 indicates the period before t.

Magnetic components X, Y and Z can be calculated from equations (1), (2) and (3):

$$X = \frac{1}{r}\frac{\partial V}{\partial \theta}, \quad Y = -\frac{1}{r\sin\theta}\frac{\partial V}{\partial \phi}, \quad Z = \frac{\partial V}{\partial r}.$$ (4)

Finally, computed magnetic components (X, Y and Z) are used for determining declination (D), inclination (I), horizontal component of the geomagnetic field (H) and total magnetic field (F):

$$H = \sqrt{X^2 + Y^2}, \quad F = \sqrt{X^2 + Y^2 + Z^2}, \quad D = \tan^{-1}\left(\frac{Y}{X}\right), \quad I = \tan^{-1}\left(\frac{Z}{H}\right).$$ (5)

Since satellite's trajectory is almost North-South, East-West variations are dominant on the mapped magnetic anomaly due to more clear variations on magnetic anomaly can be observed perpendicular to the direction of the satellite trajectories. This directional effect should be removed to revealing the orientation of the total magnetic anomaly. Therefore, the two-dimensional polynomial surface trend is fitted linearly to the data for estimating coefficients. Finally, the trend is subtracted from the total magnetic field:

$$Trend = a_1 + a_2 x + a_3 y,$$ (6)

where a_1, a_2, and a_3 are coefficients of the linear trend equation, x and y are spatial data points.

The final step is moving anomalies to the real position with Reduction To the Pole (RTP). The measured magnetic anomalies include phase shift, linked to the variation of the magnetic inclination values, and characterised by dipole nature (Fig. 3). According to Baranov and Naudy (1964) discontinuous and weak anomalies become more significant via RTP. Conversely, strong and significant anomalies are transformed into more symmetrical form after the RTP process. RTP can be quantitatively described as:

$$filter = \frac{k}{iLk_x + iMk_y + Nk} * \frac{k}{ilk_x + imk_y + nk},$$ (7)

where L, M, and N are direction cosines for the magnetisation and l, m and n are direction cosines of the magnetic field. Moreover, kx and ky are wavenumbers along x and y direction and $k = \sqrt{k_x^2 + k_y^2}$. In general, remnant magnetisation directions (L, M and N) are not known and it is assumed that remnant magnetisation and magnetic field directions are the same. Consequently, equation (7) can be rewritten as:

$$filter = \frac{k}{ilk_x + imk_y + nk} \times \frac{k}{ilk_x + imk_y + nk'} \quad \text{OR} \tag{8}$$

$$filter = \left(\frac{k}{ilk_x + imk_y + nk} \right)^2.$$

It should be noted that equation (8) is not taking into account remnant magnetisation effect. Since direction cosines of magnetisation in the study area are unknown, equation (8) is used in this study.

Normally, Reduction To the Pole (RTP) (Baranov and Naudy, 1964) could handle these problems for the higher latitudes (|latitude| > 20°). In this study, the area does not includes data points between ± 20° latitude except for the Southern part. Furthermore, the RTP process cannot apply an accurate phase shift for the large study area. Hence, alternative methods should be used instead of RTP.

2.1. Alternative method instead of the RTP process for lower latitude regions or larger study area

Roest et al. (1992) showed the amplitude of the Analytical Signal (AS) is not dependent on the magnetic inclination. AS method can extract magnetic anomalies without dipole effect and phase shift.
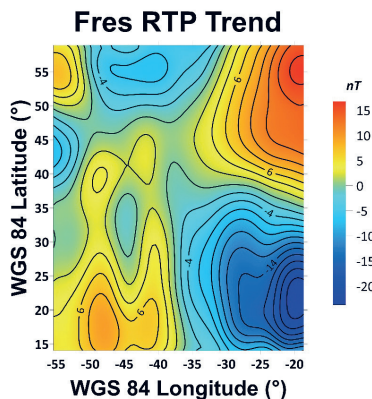

Figure 3. Total magnetic anomaly after the application of RTP and trend removal.

Analytic Signal method depends on gradients of the magnetic field along all directions. Hence amplitude of the AS for total magnetic field, T, (Nabighian, 1974) can be written as:

$$|AS(x,y)| = \sqrt{\left[\left(\frac{\partial T}{\partial x}\right)^2 + \left(\frac{\partial T}{\partial y}\right)^2 + \left(\frac{\partial T}{\partial z}\right)^2\right]}. \tag{9}$$

2.1.1. Synthetic study

In order to test the efficiency of the AS, Noise-free rectangular prism model is generated via Matlab-based Potensoft (Arısoy, 2011) code to compare the results of the RTP and the AS.

Bhattacharyya (1964) provided equation to calculate total magnetic intensity of the prism-shaped bodies:

$$\frac{F(x,y,0)}{I_p} = \left[\frac{\alpha_{23}}{2}\log\left(\frac{r_0 - \alpha_1}{r_0 + \alpha_1}\right)\right.$$
$$+ \frac{\alpha_{13}}{2}\log\left(\frac{r_0 - \beta_1}{r_0 + \beta_1}\right) - \alpha_{12}\log(r_0 + h)$$
$$- lL\tan^{-1}\left(\frac{\alpha_1\beta_1}{\alpha_1 + r_0 h + h^2}\right) \tag{10}$$
$$- mM\tan^{-1}\left(\frac{\alpha_1\beta_1}{r_0^2 + r_0 h - \alpha_1^2}\right)$$
$$\left. + nN\tan^{-1}\left(\frac{\alpha_1\beta_1}{r_0 h}\right)\right]\left|\begin{matrix}\alpha_u\\\alpha_l\end{matrix}\right.\left|\begin{matrix}\beta_u\\\beta_l\end{matrix}\right. .$$

In equation (10): $F(x,y,0)$ is total magnetic field component of the rectangular prism, x and y are coordinates of the point of the observation plane, $z = 0$ is observational plane; I_p is the polarization; L, M and N are direction cosines for the magnetisation; l, m and n are direction cosines of the magnetic field; h is the centroid depth of the prism; α and β are coordinates of the prims; α_u and α_l are upper and lower boundary conditions of α; β_u and β_l upper and lower boundary conditions of β; $\alpha_1 = \alpha - x$, $\beta_1 = \beta - x$, $\alpha^2 = \alpha_1^2 + \beta_1^2$, $r_0^2 = \alpha_1^2 + \beta_1^2 + (h - z)^2$; α_{12}, α_{13} and α_{23} can be described as:

$$\alpha_{12} = Lm + Ml; \quad \alpha_{13} = Ln + Nl \quad \alpha_{23} = Mn + nM . \tag{11}$$

Two different rectangular prims was generated. Both prism has same geometrical parameters, inclination and declination. However, one prism has a negative Total Magnetic Intensity (TMI) and the other one has a positive TMI.

The magnetic inclination and declination are –45° and –20°. Top and bottom depths of the model are 3 and 5 km, respectively (Fig. 4).

The calculated total magnetic anomalies of the rectangular prisms are shown in Fig. 5. Two prisms are inversely correlated. The generated model does not include any type of noise.

Edges of the rectangular prisms in Figs. 5a and 5b might be tracked. Nevertheless, sign of the TMI anomaly rapidly changes over lower and right edge of Fig. 5a and higher and left edge of Fig. 5b. These rapid changes may cause misinterpretation of the block model. Therefore, AS (Fig. 6) is applied to the TMI data to improve the interpretation.
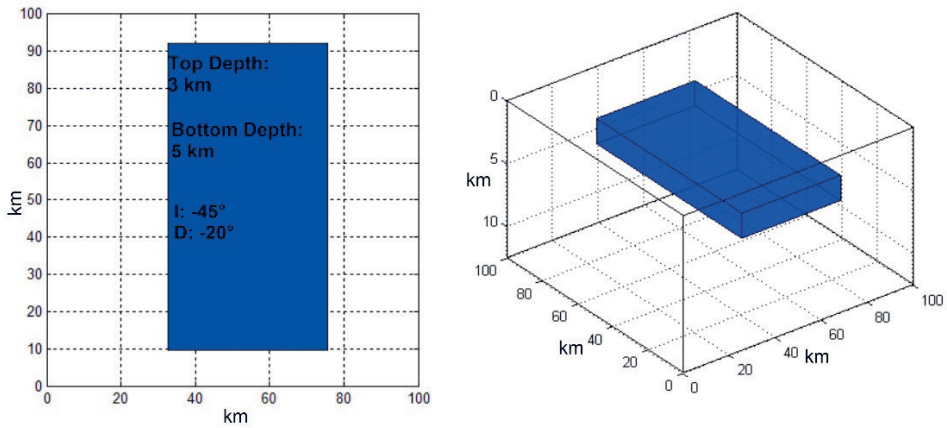

Figure 4. 2D (*left*) and 3D (*right*) illustration of the generated model. "*I*" and "*D*" are magnetic inclination and declination.
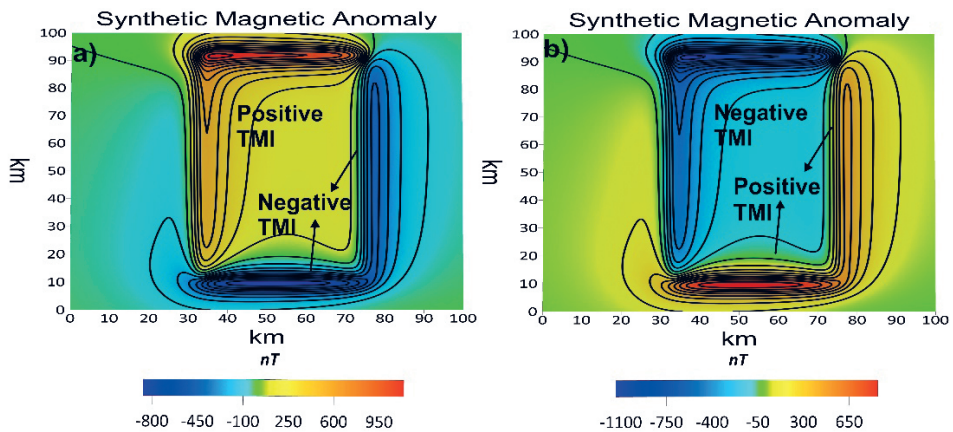

Figure 5. Total Magnetic Intensity (TMI) maps of the prisms: *a*) positive TMI is dominant, *b*) negative TMI is dominant.
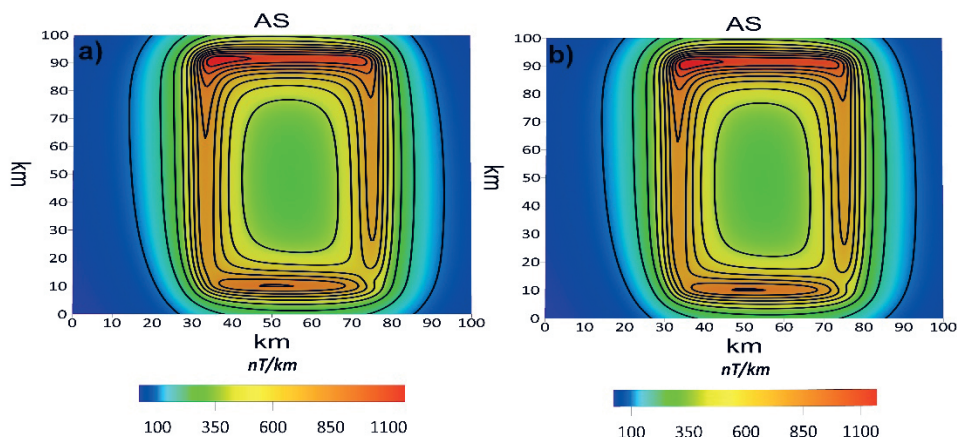
Figure 6. The AS anomalies of the rectangular prism models: *a*) positive TMI, *b*) negative TMI.

AS results of prisms provided edges clearly but it does not reflect sign of the TMI. Since Equation (9) includes square root of x, y and z gradient, AS cannot produce negative anomalies. Consequently, it might be said that AS results can only reflect gradient and intensity of the TMI anomaly.

2.2. Analytic signal results

The last step of the data processing scheme is computing the AS from the magnetic anomaly without RTP. AS of the magnetic anomaly can be used for the tectonic interpretation (Fig. 7).

Qualitatively, AS result (Fig. 7) indicates that there are three remarkable anomalies. These three anomalies will be interpreted with the auxiliary data, which are bathymetry, heat flow, fracture zones and isochrones. Isochrones are describes as equal age map and it might be considered as equipotential age points.

3. Tectonic interpretation

The AS anomaly presents regional tectonic structures over the Mid-Atlantic Ocean Ridge. Besides of the AS anomaly, heat flow map (Jessop et al., 1976), bathymetry (Smith and Sandwell, 1997) and tectonic map are used for qualitative interpretation. The tectonic map includes ridge crest (Matthews et al., 2011), fracture zones (Wessel et al., 2015) and isochrones (Müller et al., 1997). These maps are illustrated in Fig. 8. Heat flow data is available on https://www.ihfc-iugg.org/ and bathymetry data can be downloaded from https://topex.ucsd.edu/.
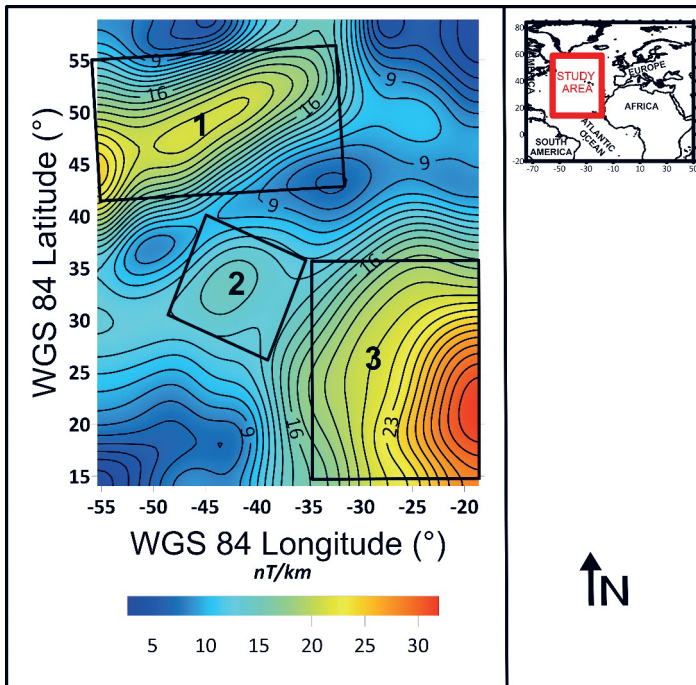
Figure 7. Analytic signal of the total magnetic field (*Fres*). The numbers on indicates: 1 - Superior Craton (SC), 2 - Minor change along the ridge crest and 3 - West African Craton (WAC).

Tectonically, the newly formed crust moves away from the ridge crest perpendicularly which results in E-W fracture zones (Smoot and Meyerhoff, 1995). The mechanism of seafloor spreading is positively correlated with the fracture zones. The seafloor spreading can be tracked on the bathymetry map. The regional fracture zones in the Mid-Atlantic Ocean Ridge can be detected by satellite magnetic data.

For the qualitative interpretation, it is worth noting that shields, cratons and the subduction zones are characterised by a higher magnetic anomaly. On the other hand, sedimentary basins and regions with thinned crust tend to produce lower magnetic anomaly (Hemant et al., 2005; Hemant and Maus, 2005). AS map indicates variations of the total magnetic anomaly. Generally, high heat flow values are observed the areas where the crust is thin or raising of the Curie isotherm.

In this study, tectonically active areas of the ridge crest are specified by high heat flow value and low AS anomaly. Figure 9 demonstrates the qualitative interpretation of the study area through bathymetry, AS, heat flow and tectonic setting map.

As it can be seen from Fig. 9, AS anomaly is decreasing where the heat flow value is high owing to the fact that high internal temperature demagnetize the

rocks. Moreover, isochrones and the ridge crest are roughly corresponding to the low AS anomaly since magnetized crust is notably thin over the ridge crest. Heat flow values are abruptly declining (see black rectangle in Fig. 9) and AS anomaly increases marginally at the region which is demonstrated its boundaries by 2nd square in Fig. 7. This increment might indicate change in magnetization gradient along the ridge crest.

Additionally, WAC could be clearly interpreted from AS anomaly whereas marginal anomaly was observed in SC. The cratonic regions produce higher AS anomaly since there is a sharp gradient in terms of magnetization.
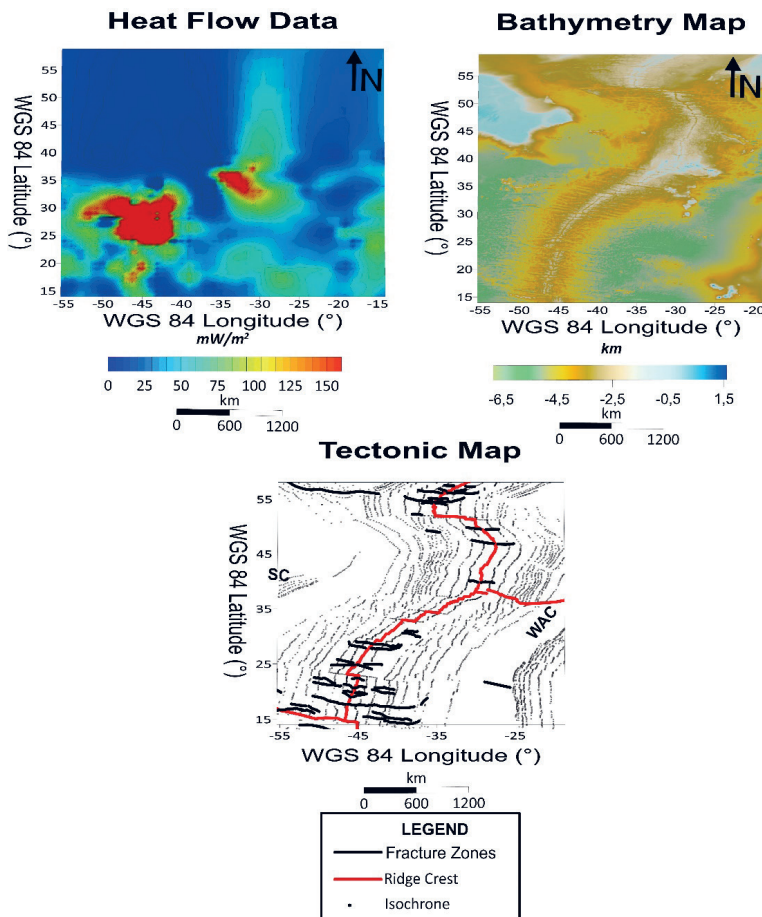

Figure 8. Heat flow map (Jessop et al., 1976), bathymetry map (Smith and Sandwell, 1997) and tectonic map, including isochrones (Müller et al., 1997), location of the ridge crest (Matthews et al., 2011) and fracture zones (Wessel et al., 2015), over the study area for the qualitative interpretation of the AS anomaly (WAC=West African Craton, SC=Superior Craton).
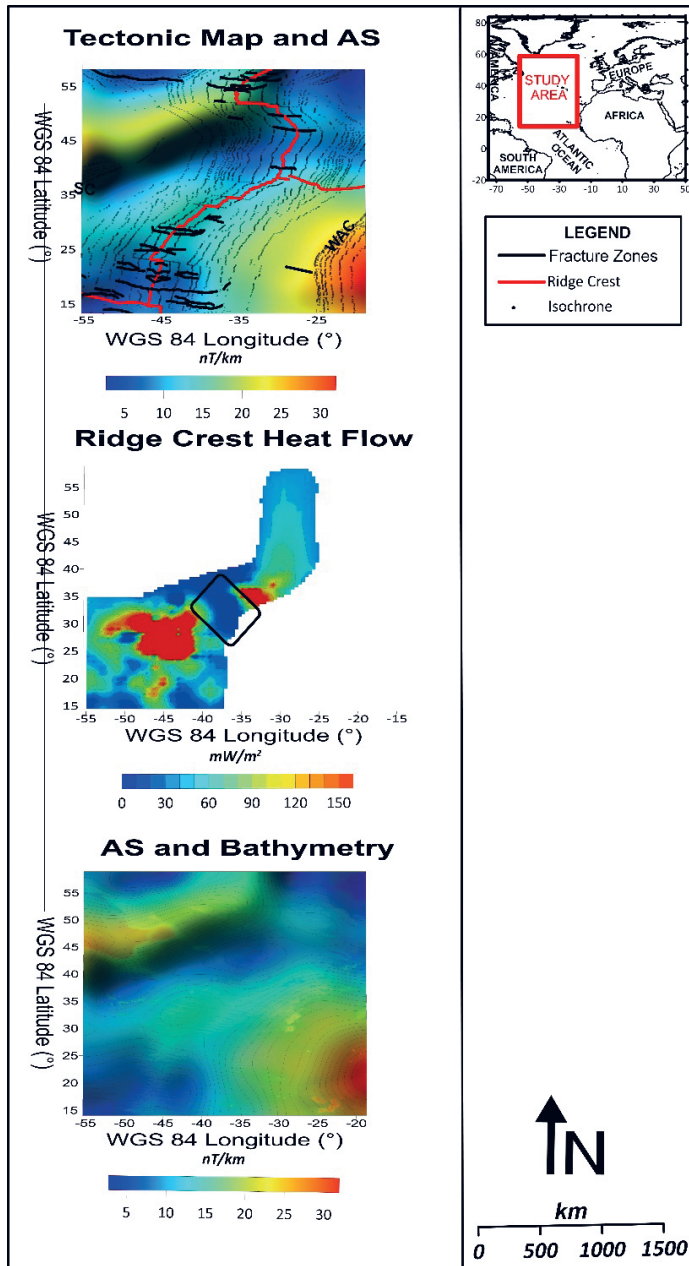
Figure 9. Combined interpretation maps of the study area (Fig. 1), which comprise a combination of AS and tectonic setting, ridge crest location and heat flow data, AS and bathymetry. The black rectangle on the ridge crest heat flow map represents noticeable decline in heat flow values along the ridge crest.
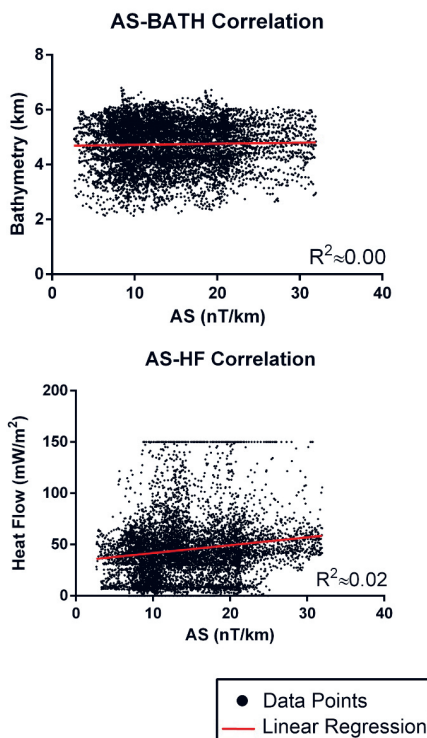
Figure 10. Correlation between AS-BATH and AS-HF.

The fracture zones cannot be interpreted on the AS anomaly since altitude of the satellites may not resolve small geological structures.

In order to detect quantitative relationship between AS (Analytic Signal), HF (Heat Flow), BATH (Bathymetry), correlation coefficients (R^2) between AS-HF and AS-BATH are analysed (Fig. 10).

As it can be seen from Fig. 10, AS-BATH and AS-HF have fairly horizontal distribution which corresponds to uncorrelated data. The R^2 value for AS-BATH plot is almost zero while correlation coefficient (R^2) of the AS-HF graph is roughly 0.02.

However, plotting all AS, HF and BATH data cannot provide representative correlation coefficients for local areas. Therefore, prominent local areas, which are 1, 2 and 3 in Fig. 7, are plotted separately with selected profiles. Direction of these profiles are perpendicular to strike of rectangle 1, 2 and 3 in Fig. 7. The chosen sections are demonstrated in Fig. 11.

It can be said that AS anomaly tends to increase in cratonic regions (see Profile 1 and Profile 3 in Fig. 11). Additionally, notable decrease in heat flow data is observed in Profiles 1 and 3. There is no significant variation in bathym-
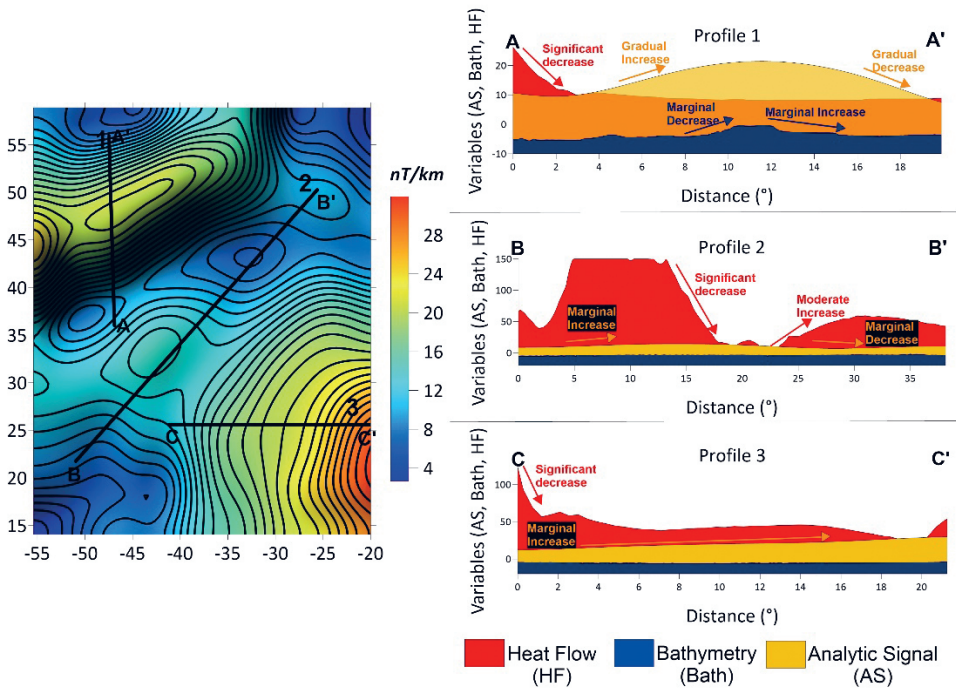
Figure 11. Profile selection and variations of AS, BATH and HF along sections. Qualitative analysis which has the same colour with the variable are indicated on the cross-sections. Profile 1, 2 and 3 correspond to rectangle 1, 2 and 3 in Fig. 7, respectively.

etry data along three sections. Instead of interpreting data only qualitatively, relationship between AS-HF and AS-BATH along these profiles are analysed quantitatively. The correlation coefficients between AS-BATH and AS-HF for each profile provided in Fig. 12.

In Fig. 12, replicated values are ignored and only unique values of each variable are used. Correlation coefficient in AS-BATH graph for Profile 1 is 0.80 which indicates these two variables are somewhat correlated. Additionally, AS lower than 13 nT/km and higher than 20 nT/km dispersion of AS and BATH values are quite high. If AS-HF plot for Profile 1 is evaluated, two variables are highly correlated till 20 nT/km threshold. After 12 nT/km, heat flow values are dramatically rising.

Profile 2 roughly corresponds to the ridge crest. AS-BATH correlation at this section is quite high, 0.90. The non-extreme values of the AS linearly fit to the BATH values. However, AS > 13 nT/km and AS < 7 nT/km have notable deviations respect to the linear fit. It can be said that if AS has considerably low and high values, BATH is exponentially decreasing and rising respectively. AS and

HF for Profile 2 can be evaluated as well-correlated variables with $R^2 = 0.88$. AS-HF graph consistently follows the linear fit from 7 nT/km to 10 nT/km. After 10 nT/km, AS values are gradually increasing while HF values are rising dramatically.

Profile 3 is used for analysis correlation between AS, HF and BATH for WAC. AS-BATH variables are remarkably correlated with $R^2 = 0.93$. However AS values less than approximately 13 nT/km show lower correlation with BATH values.
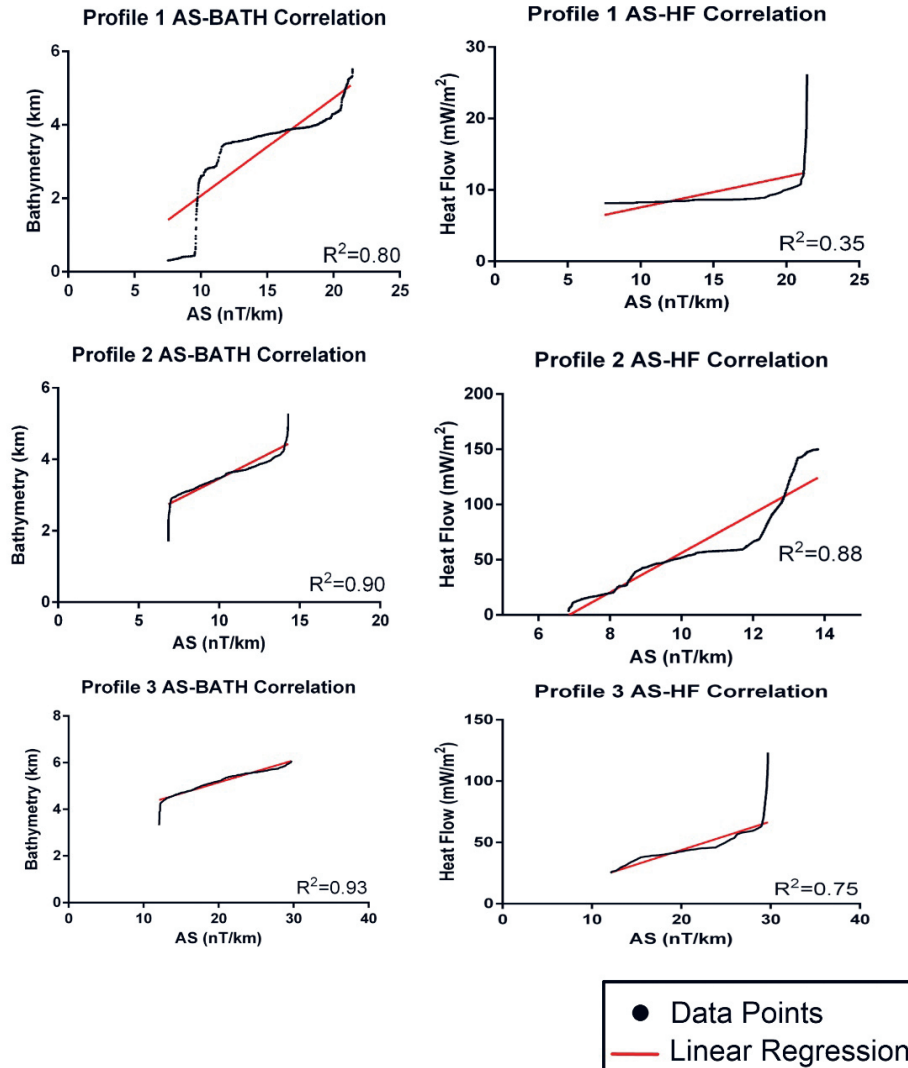

Figure 12. Correlation coefficients between variables for each profile.

AS-HF graph can be considered as moderately correlated ($R^2 = 0.75$). Although AS and HF variables have a moderate correlation, these variables are distributed along linear regression line for AS < 30 nT/km. Higher values of AS (AS > 30 nT/km) indicates rapid increase in heat flow values.

4. Discussion

The size of the chosen study area is a prominent factor for the pre-processing scheme. RTP results might converge inaccurate phase shifts over the large study area. On the other hand, the smaller study area, respect to the wavelength of the satellite magnetic data, cannot be used as the resolution issues of the satellite magnetic data. For the small study area, regional tectonic structures may not be able to be detected due to the observation altitude of the magnetic data.

The measured raw magnetic data cannot be used for the interpretation of the geological structures due to the dominancy of the core magnetic field. Therefore, IGRF correction and trend removal are applied to the raw data. Once the IGRF model ($n = 13$) is subtracted from the data, total magnetic intensity anomaly (Fig. 2) is obtained and the crustal discontinuities related to the tectonic setting can be analysed. Moreover, diurnal effects of the external magnetic field are tried to be filtered by constraining Kp index.

If RTP (Fig. 2) and AS (Fig. 7) anomalies are compared, AS anomaly is better than RTP in terms of representation of the tectonic elements. Interestingly, RTP anomaly approximately changes between 0 nT and 15 nT at the ridge crest and it has range from 0 nT to –22 nT at the cratonic regions. Ridge crest and cratonic regions cannot be interpreted precisely on the RTP anomaly. The results of RTP are unable to indicate continuity of the regional tectonic structures. Hence, it is proved that the RTP process does not provide an accurate phase shift over the large study area. Unlike the RTP anomaly, the AS anomaly reflects edges and characteristics of the WAC clearly but SC cannot be resolved as the WAC.

The synthetic study showed that AS anomaly is one of the applicable alternatives where the RTP process does not work. The other alternative is the Local Wavenumber Method (LW) (Phillips, 2000). For the low-resolution data, however, the LW method may not produce as interpretable results as the AS method. Since second derivatives of the measured field required in LW method, the data spacing should be very small. In the satellite magnetic data spacing is quite large across satellite trajectories. Therefore, the AS method is preferred instead of LW.

The tectonic setting (Fig. 8) of the study area is quite complex. Maximum heat flow values are observed around (–45° W, 30° N) and (–33° W, 35° N). These regions might correspond to the major tectonic activities of the seafloor spreading

mechanism. The NW part of the heat flow map where SC located is characterised by low heat flow values.

The frequency of E-W fracture zones is increased around (–45° W, 30° N) where heat flow values are high. These fracture zones can be tracked on the bathymetry map. Water bottom depth indicates regions around the ridge crest has a complex characteristic while cratonic regions produce smooth variations.

The equal age map has a prominent contribution to the qualitative interpretation. The age of the crust is not varying along the N-S trajectory for the single isochrone. From the distribution of the isochrones, two major crustal zones in terms of ages can be identified. The first crustal zone is around the ridge crest and the second zone is around the cratons.

The processed satellite magnetic anomaly, AS, effectively reflects active seafloor spreading regions over the Mid-Atlantic Ocean ridge crest. The AS anomaly is notably consistent with the other data, which are bathymetry, tectonic setting map and heat flow (Fig. 9).

The isochrones along the ridge crest correspond to the lower AS anomaly. On the other hand, the location of the higher AS anomaly and isochrones over the cratons are considerably consistent.

 The ridge crest heat flow map provides regions with relatively high heat flow, around (–45° W, 30° N) and (–33° W, 35° N), along the crest. For the study area, the notably higher heat flow is likely to indicate newly forming an oceanic crust or active tectonic areas. However, there is a sharp decrease in heat flow between (–45° W, 30° N) and (–33° W, 35° N). This area might be associated with a passive tectonic region on the ridge crest.

The integrated interpretation of the AS anomaly and bathymetry provides the location of the complex and passive tectonic areas. Through the ridge crest where the AS anomaly decreases, water bottom depth variations are considerable. On the contrary, smooth bathymetric variations and high AS anomaly are observed over the cratonic regions.

Regarding to quantitative interpretation, the results are summarised as;

– Profile 1: Extreme values of AS (AS < 13 nT/km and AS > 20 nT/km for AS-BATH plot and AS > 20 nT/km for AS-HF graph) shows significantly less correlation along the SC region.

– Profile 2: AS-BATH graph showed substantially high correlation ($R^2 = 0.90$) along the ridge crest where AS is higher than 7 nT/km and lower than 13 nT/km. On the other hand, AS-HF plot only consistent with linear fit from 7 nT/km to 10 nT/km. Even though high correlation ($R^2 = 0.88$) is observed, increasing rate of two variables are quite different after 10 nT/km threshold.

– Profile 3: AS and BATH values are fairly well-correlated ($R^2 = 0.93$) for WAC region. However, lower values of AS (AS < 13 nT/km) are not showing

consistency with BATH. Despite the fact that AS-HF reflects moderate correlation, the variables are well-distributed on the linear regression line for AS values less than 30 nT/km.

On the whole, in cratonic regions (Profiles 1 and 3), AS-HF variables are increasing consistently until 20 nT/km and 30 nT/km for Profile 1 and 3 respectively. Although low correlation (0.35) is observed in Profile 1, it is resulted from rapid increase in heat flow after AS = 20 nT/km. Along the ridge crest (Profile 2), AS-BATH values remarkably distributed ($R^2 = 0.90$) on the linear fit. Consequently, it can be said that increasing rate in AS and HF variables are correlated in cratonic region whereas AS-BATH plot indicates coherency along the ridge crest.

5. Conclusion

Regional tectonic features and heat flow variations over the Mid-Atlantic Ridge are represented by Swarm-A magnetic data. Additionally, detailed description of processing scheme, including filtering data that correspond to the magnetically quiet time, subtracting IGRF field, trend removal and AS, of the satellite magnetic data is presented.

If results of AS and RTP are compared, AS anomaly enhances the interpretation of the tectonic boundaries. Moreover, the RTP process is far from being applicable for this study.

In quantitative manner, three cross-sections are obtained from the study area to evaluate the correlation coefficients between BATH and HF respect to AS. The computed AS-BATH correlations are 0.80, 0.90 and 0.93 for Profile 1, Profile 2 and Profile 3 respectively. Additionally, 0.35 (Profile 1), 0.88 (Profile 2) and 0.75 (Profile 3) are obtained from AS-HF plot.

References

Abramova, D. Y., Filippov, S. V., Abramova, L. M., Varentsov, I. M. and Lozovskii, I. N. (2016): Changes of lithospheric magnetic anomalies with altitude (According to the CHAMP satellite), *Geomagn. Aeronomy*, **56**, 239–248, https://doi.org/10.1134/S001679321602002X.

Akhoondzadeh, M., De Santis, A., Marchetti, D., Piscini, A. and Cianchini, G. (2018): Multi precursors analysis associated with the powerful Ecuador (M_W=7.8) earthquake of 16 April 2016 using Swarm satellites data in conjunction with other multi-platform satellite and ground data, *Adv. Space Res.*, **61**, 248–263, https://doi.org/10.1016/j.asr.2017.07.014.

Arısoy, M. Ö. and Dikmen, Ü. (2011): Potensoft: MATLAB-based software for potential field data processing, modeling and mapping, *Comput. Geosci.*, **37**, 935–942, https://doi.org/10.1016/j.cageo.2011.02.008.

Arkani-Hamed, J., Langel, R. A. and Purucker, M. (1994): Scalar magnetic anomaly maps of Earth derived from POGO and Magsat data, *J. Geophys. Res. – Sol. Ea.*, **99**(B12), 24075–24090, https://doi.org/10.1029/94JB00930.

Baranov, V. and Naudy, H. (1964): Numerical calculation of the formula of reduction to the magnetic pole, *Geophysics*, **29**, 67–79, https://doi.org/10.1190/1.1439334.

Bhattacharyya, B. K. (1964): Magnetic anomalies due to prism-shaped bodies with arbitrary polarization, *Geophysics*, **29**, 517–531, https://doi.org/10.1190/1.1439386

Bokelmann, G. H. and Wüstefeld, A. (2009): Comparing crustal and mantle fabric from the North American craton using magnetics and seismic anisotropy, *Earth Planet. Sci. Lett.*, **277**, 355–364, https://doi.org/10.1016/j.epsl.2008.10.032.

Cain, J.C., Wang, Z., Kluth, C. and Schmitz, D. R. (1989): Derivation of a geomagnetic model to *n* = 63, *Geophys. J. Int.*, **97**, 431–441, https://doi.org/10.1111/j.1365-246X.1989.tb00513.x.

Civet, F., Thébault, E., Verhoeven, O., Langlais, B. and Saturnino, D. (2015): Electrical conductivity of the Earth's mantle from the first Swarm magnetic field measurements, *Geophys. Res. Lett.*, **42**, 3338–3346, https://doi.org/10.1002/2015GL063397.

Friis-Christensen, E., Lühr, H. and Hulot, G. (2006): Swarm: A constellation to study the Earth's magnetic field, *Earth Planets Space*, **58**, 351–358, https://doi.org/10.1186/BF03351933.

Gibson, R. I. and Millegan, P. S. (1998): *Geologic applications of gravity and magnetics: Case histories*. Society of Exploration Geophysicists and American Association of Petroleum Geologists.

Hemant, K. and Maus, S. (2005): Geological modeling of the new CHAMP magnetic anomaly maps using a geographical information system technique, *J. Geophys. Res. – Sol. Ea.*, **110**(B12), https://doi.org/10.1029/2005JB003837.

Hemant, K., Maus, S. and Haak, V. (2005): Interpretation of CHAMP crustal field anomaly maps using Geographical Information System (GIS) technique, *Earth Observation with CHAMP*, 249–254.

Hildenbrand, T. G., Berger, B., Jachens, R. C. and Ludington, S. (2000): Regional crustal structures and their relationship to the distribution of ore deposits in the western United States, based on magnetic and gravity data, *Econ. Geol.*, **95**, 1583–1603, https://doi.org/10.2113/gsecongeo.95.8.1583.

Jessop, A. M., Hobart, M. A. and Sclater, J. G. (1976): The world heat flow data collection—1975, Geothermal Series. *Earth Physics Branch, Energetic Mines and Resources, Ottawa*.

Langel, R., Ousley, G., Berbert, J., Murphy, J. and Settle, M. (1982): The MAGSAT mission, *Geophys. Res. Lett.*, **9**, 243–245, https://doi.org/10.1029/GL009i004p00243.

Langel, R. A. and Hinze, W. J. (1998): *The magnetic field of the Earth's lithosphere: The satellite perspective*. Cambridge University Press.

Matthews, K. J., Müller, R. D., Wessel, P. and Whittaker, J. M. (2011): The tectonic fabric of the ocean basins, *J. Geophys. Res. – Sol. Ea.*, **116**(B12), https://doi.org/10.1029/2011JB008413.

Maus, S., Yin, F., Lühr, H., Manoj, C., Rother, M., Rauberg, J., Michaelis, I., Stolle, C. and Müller, R. D. (2008): Resolution of direction of oceanic magnetic lineations by the sixth-generation lithospheric magnetic field model from CHAMP satellite magnetic measurements, *Geochem. Geophy. Geosys.*, **9**, https://doi.org/10.1029/2008GC001949.

Mayaud, P. N. (1980): The *Dst* index, *Derivation, Meaning, and Use of Geomagnetic Indices*, **22**, 115–129, https://doi.org/10.1002/9781118663837.ch8.

Moretto, T., Vennerstrom, S., Olsen, N., Rastätter, L. and Raeder, J. (2006): Using global magnetospheric models for simulation and interpretation of Swarm external field measurements, *Earth Planets Space*, **58**, 439–449, https://doi.org/10.1186/BF03351940.

Müller, R. D., Roest, W. R., Royer, J. Y. and Sclater, J. G. (1997): Digital isochrones of the world's ocean floor, *J. Geophys. Res.*, **102**(B2), 3211–3214.

Nabighian, M. N., (1974): Additional comments on the analytic signal of two-dimensional magnetic bodies with polygonal cross-section, *Geophysics*, **39**, 85–92, https://doi.org/10.1190/1.1440416.

Nakanishi, M., Tamaki, K. and Kobayashi, K. (1992): Magnetic anomaly lineations from Late Jurassic to Early Cretaceous in the west-central Pacific Ocean, *Geophys. J. Int.*, **109**, 701–719, https://doi.org/10.1111/j.1365-246X.1992.tb00126.x.

Olsen, N., Holme, R., Hulot, G., Sabaka, T., Neubert, T., Tøffner-Clausen, L., Primdahl, F., Jørgensen, J., Léger, J. M., Barraclough, D. and Bloxham, J. (2000): Ørsted initial field model, *Geophys. Res. Lett.*, **27**, 3607–3610, https://doi.org/10.1029/2000GL011930.

Olsen, N., Lühr, H., Sabaka, T. J., Mandea, M., Rother, M., Tøffner-Clausen, L. and Choi, S. (2006): CHAOS—a model of the Earth's magnetic field derived from CHAMP, Ørsted, and SAC-C magnetic satellite data, *Geophys. J. Int.*, **166**, 67–75, https://doi.org/10.1111/j.1365-246X.2006.02959.x.

Phillips, J. D. (2000): Locating magnetic contacts: A comparison of the horizontal gradient, analytic signal, and local wavenumber methods, *SEG Technical Program Expanded Abstracts 2000*, 402–405, https://doi.org/10.1190/1.1816078.

Purucker, M. and Whaler, K. (2007): Crustal magnetism, *Treatise on Geophysics*, **5**, 195–237.

Ravat, D., Langel, R. A., Purucker, M., Arkani-Hamed, J. and Alsdorf, D. E. (1995): Global vector and scalar Magsat magnetic anomaly maps, *J. Geophys. Res. – Sol. Ea.*, **100(B10)**, 20111–20136, https://doi.org/10.1029/95JB01237.

Regan, R. D., Cain, J. C. and Davis, W. M. (1975): A global magnetic anomaly map, *J. Geophys. Res.*, **80**, 794–802, https://doi.org/10.1029/JB080i005p00794.

Roest, W. R., Verhoef, J. and Macnab, R. (1995): Magnetic anomalies and tectonic elements of northeast Eurasia, *GSC Open File*, *2574*.

Roest, W. R., Verhoef, J. and Pilkington, M. (1992): Magnetic interpretation using the 3-D analytic signal, *Geophysics*, **57**, 116–125, https://doi.org/10.1190/1.1443174.

Smith, W. H. and Sandwell, D. T. (1997): Global sea floor topography from satellite altimetry and ship depth soundings, *Science*, **277(5334)**, 1956–1962, https://doi.org/10.1126/science.277.5334.1956.

Smoot, N. C. and Meyerhoff, A. A. (1995): Tectonic fabric of the Atlantic Ocean floor: speculation vs. reality, *J. Petrol. Geol.*, **18**, 207–222, https://doi.org/10.1111/j.1747-5457.1995.tb00898.x.

Taylor, P. T., Kis, K., Toronyi, B., Puszta, S. and Wittmann, G. (2019): Interpretation of the magnetic measurements of the Swarm-A Satellite over Central Europe, *Int. J. Astronaut Aeronautical Eng.*, **4**, 029.

Taylor, P. T., Kis, K. I. and Wittmann, G. (2014): Satellite-altitude horizontal magnetic gradient anomalies used to define the Kursk magnetic anomaly, *J. Appl. Geophys.*, **109**, 133–139, https://doi.org/10.1016/j.jappgeo.2014.07.018.

Thébault, E., Finlay, C.C., Beggan, C.D., Alken, P., Aubert, J., Barrois, O., Bertrand, F., Bondar, T., Boness, A., Brocco, L. and Canet, E. (2015): International geomagnetic reference field: The 12th generation, *Earth Planets Space*, **67**, 79, https://doi.org/10.1186/s40623-015-0228-9.

Wessel, P., Matthews, K. J., Müller, R. D., Mazzoni, A., Whittaker, J. M., Myhill, R. and Chandler, M. T. (2015): Semiautomatic fracture zone tracking, *Geochem. Geophys. Geosys.*, **16**, 2462–2472, https://doi.org/10.1002/2015GC005853.

SAŽETAK

Tumačenje magnetskih anomalija nad Srednjeatlantskim grebenom satelitom Swarm-A

Ilkin Özsöz i Oya Ankaya Pamukçu

U ovom se radu raspravlja o postupcima i tumačenju magnetskih podataka izmjerenih nad Srednje-atlantskim grebenom satelitom Swarm-A. Postupak obrade podataka ima četiri faze nakon pretvorbe podatkovnog formata. Prva faza je odabir podataka čiji je indeks Kp manji od 1. Drugo, doprinos glavnog magnetskog polja treba oduzeti od izmjerenih podataka, na primjer koristeći IGRF model. Nakon ovog koraka slijedi uklanjanje trenda, vezanog uz putanju satelita. Posljednji korak je uklanjanje dipolnog karaktera magnetskog polja putem redukcije na pol (RTP). Unatoč tome, RTP proces može uzrokovati pogrešno tumačenje na velikom području istraživanja i nižim geografskim širinama. Stoga se koristila amplituda analitičkog signala (AS) kao alternativa RTP-u.

Kvalitativno tumačenje magnetske anomalije provodilo se pomoću AS anomalije, batimetrije, toplinskog toka i tektonske karte. Kvantitativni koeficijenti korelacije batimetrije i toplinskog toka tumačeni su obzirom na AS.

Ključne riječi: SWARM, obrada magnetskih podataka, analitički signal, kvalitativna i kvantitativna interpretacija

Corresponding author's address: Ilkin Özsöz, General Directorate of Mineral Research and Exploration, Marine Research Department, Ankara, Turkey; e-mail: ilkin.ozsoz@mta.gov.tr